Electrocatalytic Oxygen Reduction

Enzyme-Inspired Iron Porphyrins for Improved Electrocatalytic Oxygen Reduction and Evolution Reactions

Lisi Xie[+], Xue-Peng Zhang[+], Bin Zhao, Ping Li, Jing Qi, Xinai Guo, Bin Wang, Haitao Lei, Wei Zhang, Ulf-Peter Apfel, and Rui Cao*

***Abstract:** Nature uses Fe porphyrin sites for the oxygen reduction reaction (ORR). Synthetic Fe porphyrins have been extensively studied as ORR catalysts, but activity improvement is required. On the other hand, Fe porphyrins have been rarely shown to be efficient for the oxygen evolution reaction (OER). We herein report an enzyme-inspired Fe porphyrin **1** as an efficient catalyst for both ORR and OER. Complex **1**, which bears a tethered imidazole for Fe binding, beats imidazole-free analogue **2**, with an anodic shift of ORR half-wave potential by 160 mV and a decrease of OER overpotential by 150 mV to get the benchmark current density at $10\,mA\,cm^{-2}$. Theoretical studies suggested that hydroxide attack to a formal $Fe^{V}=O$ form the O−O bond. The axial imidazole can prevent the formation of trans $HO-Fe^{V}=O$, which is less effective to form O−O bond with hydroxide. As a practical demonstration, we assembled rechargeable Zn-air battery with **1**, which shows equal performance to that with Pt/Ir-based materials.*

Nature uses Fe porphyrin heme sites to activate and reduce O_2.[1,2] Specifically, O_2 reduction to water, as mediated by cytochrome *c* oxidases (C*c*Os), is a vital process in respiration.[1,3] Inspired by nature, many synthetic Fe porphyrins and other related metal macrocycles have been designed and investigated as catalysts for O_2 reduction.[4–18] From these studies, fundamental knowledge to boost catalyst performance is learned. For example, efficient electron transfer to Fe porphyrin sites and proper hydrogen bonding interactions with Fe-O_2 adducts can facilitate the 4e reduction of O_2 to water.[11,19–24] However, despite these achievements in improving selectivity, Fe porphyrins in general showed moderate electrocatalytic ORR activity with half-wave potential

< 0.80 V versus reversible hydrogen electrode (RHE).[10,11,14,25,26] Thus, ORR activity improvement of molecular Fe porphyrins is required.

In the structure of C*c*Os, there is a histidine imidazole group binding to the axial position of Fe (Figure 1 a). Synthetic modeling studies from Collman[19] and Dey[27] demonstrated that this axial imidazole can increase electron density on Fe through a so-called "push effect". This effect is favorable for O_2 binding and more importantly can assist the O−O bond cleavage by increasing pK_a of oxygen atoms of the resulted Fe-O_2 adduct, which leads to both improved activity and selectivity for O_2 reduction to water. Recently, by using Fe phthalocyanines and Co corroles, electron-donating axial ligands have also been reported to improve ORR activity by notably shifting ORR half-wave potentials to the anodic direction by Cho,[28] Zagal,[29] and us.[30] Therefore, results from natural and artificial examples suggested that proper axial ligands on Fe porphyrins will promote electrocatalytic ORR performance in terms of both activity and selectivity.

[*] L. S. Xie,[+] Dr. X.-P. Zhang,[+] B. Zhao, P. Li, Dr. J. Qi, X. A. Guo, Dr. B. Wang, Dr. H. T. Lei, Prof. Dr. W. Zhang, Prof. Dr. R. Cao
Key Laboratory of Applied Surface and Colloid Chemistry, Ministry of Education, School of Chemistry and Chemical Engineering, Shaanxi Normal University
Xi'an 710119 (China)
E-mail: ruicao@snnu.edu.cn

Prof. Dr. U.-P. Apfel
Ruhr-Universität Bochum, Fakultät für Chemie und Biochemie, Anorganische Chemie I
Universitätsstrasse 150, 44801 Bochum (Germany)
and
Fraunhofer UMSICHT
Osterfelder Strasse 3, 46047 Oberhausen (Germany)

[+] These authors contributed equally to this work.

Supporting information and the ORCID identification number(s) for the author(s) of this article can be found under:
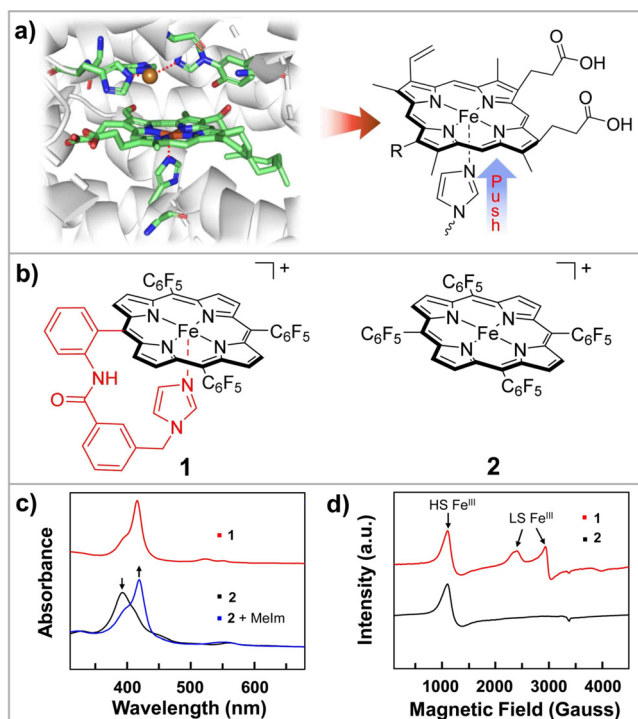https://doi.org/10.1002/anie.202015478.

Figure 1. a) Diagram showing the electronic "push effect" of the *trans* axial histidine imidazole group in C*c*Os. b) Molecular structure of Fe porphyrins **1** and **2** used in this work. c) UV/Vis spectra of **1**, **2**, and **2** added with one equivalent of methylimidazole (MeIm) in THF. d) X-band EPR data of **1** and **2** in THF at 100 K.

On the other hand, Fe porphyrins have been rarely shown to be efficient for OER. Metal porphyrins, including Co,[31,32] Ni,[33–35] and Cu,[36] have been reported to be able to electrocatalyze water oxidation to evolve O_2 with low overpotentials. Unlike these metal porphyrins, Fe porphyrin analogues are much less efficient for OER electrocatalysis, although molecular Fe complexes of other N-based ligands have been shown to be highly active for water oxidation.[37–43] Considering that water oxidation to O_2 is the reverse reaction of O_2 reduction, we propose that the catalytic OER feature of Fe porphyrins can be significantly improved if their structures can be properly designed.

Based on these considerations, we herein report an enzyme-inspired Fe porphyrin **1** (Figure 1b) as an efficient electrocatalyst for both ORR and OER. By tethering an imidazole group for Fe binding, the resulted coordination structure of Fe in **1** resembles that in C*c*Os. Importantly, **1** represents an unparalleled example of bifunctional Fe porphyrins for efficient ORR and OER. Control experiments using analogue **2**, which lacks the axial imidazole ligand, further underlines the critical role of tethered imidazole in boosting ORR and OER. To demonstrate the practical use, we assembled Zn-air battery with **1**, which shows equal performance to that with Pt/Ir-based materials. Note that only few molecular complexes can catalyze both ORR and OER under the same conditions with high efficiency and durability,[44] a feature required for rechargeable Zn-air batteries.[45–50] By precisely modifying molecular structures, this work underlines unique benefits and potential applications of molecular electrocatalysis in new energy technologies.

Fe porphyrins **1** and **2** were synthesized (detailed synthetic procedures were descried in the Supporting Information). The identity and purity of triflate (OTf) salts of **1** and **2** were proved by high-resolution mass spectrometry (Figures S9, S10) and by elemental analysis. In the structure of **1**, the binding of tethered imidazole on Fe was confirmed. As shown in Figure 1c, UV/Vis spectra of **1** and **2** display different Soret bands, indicating their dissimilar coordination structures. Importantly, with the addition of one equivalent of methyl-imidazole, the UV/Vis spectrum of **2** became almost identical to that of **1**. On the other hand, we can detach tethered imidazole from Fe in **1** by adding excess AgOTf, as Ag^+ ions can competitively bind with imidazoles. The resulted UV/Vis spectrum of **1** turned to be similar to that of **2** (Figure S11). Note that addition of excess NaOTf caused negligible changes to the UV/Vis spectrum of **1** (Figure S12). Moreover, the electron paramagnetic resonance (EPR) spectrum of **1** showed both high-spin (HS) and low-spin (LS) Fe^{III} states, while **2** showed only HS Fe^{III} state (Figure 1d). We propose that for the Fe^{III} ion of **1**, in addition to the axial imidazole group, the OTf counter anion may bind and unbind with Fe, leading to an equilibrium between six-coordinate LS and five-coordinate HS Fe^{III} states.[51,52] Similar to UV/Vis studies, with addition of one equivalent of methylimidazole, the EPR spectrum of **2** became identical to that of **1** (Figure S13), suggesting the binding of imidazole on Fe. When excess AgOTf was added to **1**, the LS Fe^{III} signals disappeared, which was consistent with the detaching of the tethered imidazole from Fe (Figure S14). With the addition of NaOTf, the ratio of

LS:HS Fe^{III} of **1** increased (Figure S15), confirming the equilibrium between binding and unbinding of OTf anions on Fe. All these results demonstrate that tethered imidazole in **1** binds with Fe.

Carbon nanotubes (CNTs) were used as supporting materials for electrocatalysis (Figure S16). Fe porphyrins were loaded on CNTs through physical adsorption to give **1**/CNT and **2**/CNT (details for preparation were described in Supporting Information). The resulted hybrids were characterized by scanning electron microscopy (SEM) and transmission electron microscopy (TEM), showing no aggregated particles (Figures 2a,b, and S17–19). The successful loading of Fe porphyrins on CNTs was confirmed by energy-dispersive X-ray (EDX) elemental mappings (Figures 2c and S19), line-scan imaging analyses (Figures S20, S21), and infrared (Figure 2d) and X-ray photon electron spectroscopy (XPS, Figure S22). In XPS, the spectrum of **1**/CNT in the Fe 2p region showed two peaks at 711.3 and 724.6 eV with two satellites, which could be assigned to Fe $2p_{3/2}$ and Fe $2p_{1/2}$, respectively.[53,54] For **2**/CNT, these two signals were at 711.6 and 724.9 eV, respectively. As compared to **2**/CNT, the small but significant shift of 0.3 eV to the lower energy direction observed for Fe signals of **1**/CNT is consistent with the axial imidazole binding, which led to increased electron density on Fe in **1**. All these results confirm the loading of intact molecules of **1** on CNTs.

Electrocatalytic ORR was evaluated in 0.1 M KOH solutions. The cyclic voltammogram (CV) of **1**/CNT in N_2- and O_2-saturated electrolytes confirmed its ORR activity (Figure S23), and showed that its performance is superior to that of **2**/CNT and CNTs under the same conditions. Note that all potentials reported in this work are referenced to RHE. The ORR activity was also examined by rotating ring-disk electrode (RRDE) measurements. The linear sweep voltammogram (LSV) of **1**/CNT displays an ORR wave with an onset potential $E_{onset} = 930$ mV (measured at current density

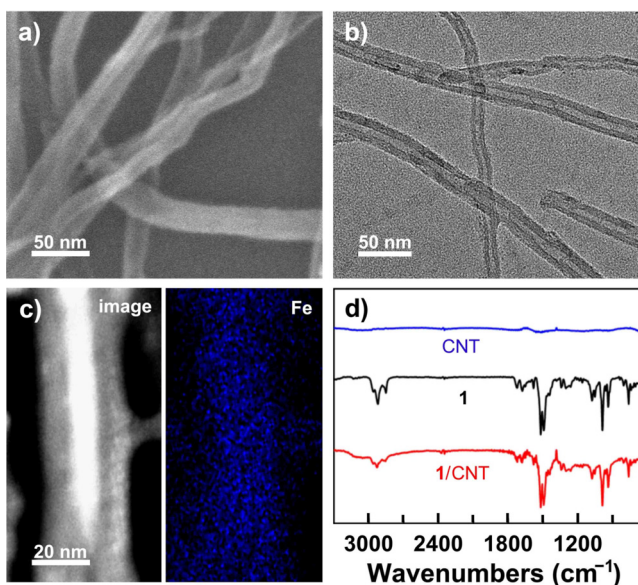***Figure 2.*** a) SEM, b) TEM, and c) EDX elemental mapping images of **1**/CNT. d) Infrared spectra of CNT, **1**, and **1**/CNT.

$0.10\ \mathrm{mA\,cm^{-2}}$) and a half-wave potential $E_{1/2} = 840\ \mathrm{mV}$ (Figure 3 a), representing state-of-the-art catalytic ORR activity as compared to reported Fe porphyrins and other Fe-based molecular catalysts (Table S1). For **2**/CNT, these values are $E_{\mathrm{onset}} = 850\ \mathrm{mV}$ and $E_{1/2} = 680\ \mathrm{mV}$. This large 160-mV anodic shift of ORR half-wave potential highlights the critical role of tethered imidazole group on boosting ORR electrocatalysis. The ORR turnover frequency (TOF) with **1**/CNT was estimated to be $0.49\ \mathrm{s^{-1}}$ at 0.8 V per Fe site. This value is much larger than that of **2**/CNT ($0.062\ \mathrm{s^{-1}}$ at 0.8 V). Comparison with previously reported molecular catalysts under similar conditions also demonstrates the high ORR activity of **1**/CNT.[23,25,29,55–59] Note that unmodified CNTs have very poor electrocatalytic ORR activity (Figure 3 a).

Next, the number (n) of electrons transferred per O$_2$ molecule with **1**/CNT was determined to be 3.97 based on RRDE results, while it was 3.84 with **2**/CNT (Figure 3 b). Similar n values were obtained by using Koutecky–Levich (K–L) analyses (Figures S24, S25).[60,61] The durability of **1**/CNT was then evaluated, showing almost no loss of electrocatalytic ORR activity after 1000 CV cycles (Figure 3 c). In prolonged electrolysis, the catalytic ORR current with **1**/CNT dropped only by $< 6\%$ after 10 h (Figure S26). UV/Vis (Figure S27) and XPS (Figure S28) spectra of **1**/CNT before and after durability tests are almost identical, confirming its high stability during ORR electrocatalysis.

In addition to ORR, electrocatalytic OER was also evaluated in 0.1 M KOH. As shown in Figure 3 d, **1**/CNT is active for OER and can reach the benchmark current density of $10\ \mathrm{mA\,cm^{-2}}$ at 500 mV overpotential, which is superior to **2**/CNT ($\eta_{10} = 650\ \mathrm{mV}$). Unmodified CNTs displayed poor activity for OER under the same conditions (Figure S29). By normalizing OER activity with the electrochemical surface area (ECSA, Figure S30),[62] **1**/CNT is still much more active than **2**/CNT (Figure S31). Because **1** and **2** have almost identical structures except that **1** bears a tethered imidazole for Fe binding, this large activity difference observed between these two complexes underlines the critical role of the axial imidazole in boosting OER electrocatalysis. It is worth noting that the OER performance of **1** is superior to that obtained with other molecular catalysts functioning under similar conditions (Table S2).

We can estimate the OER TOF per Fe site of **1**/CNT to be $0.54\ \mathrm{s^{-1}}$ at $\eta = 570\ \mathrm{mV}$, which is larger than that of **2**/CNT ($0.17\ \mathrm{s^{-1}}$ at $\eta = 570\ \mathrm{mV}$) and other molecular catalysts functioning under similar conditions.[63–65] The Tafel slope of **1**/CNT was 84 mV/dec (Figure S32), while it was 110 mV/dec for **2**/CNT, implying more favourable catalytic kinetics with **1**/CNT. Next, we examined the stability of **1**/CNT for OER by bulk electrolysis with an applied overpotential of $\eta = 490\ \mathrm{mV}$. As shown in Figure 3 e, during 8 h electrolysis, the OER current maintained stable. The slight ($< 7\%$) current decrease is due to pH decrease of the solution (from 13.00 to 12.86). Moreover, the accumulated charge during electrolysis displayed a linear dependence on time (Figure S33). After OER electrolysis, **1**/CNT was applied to ORR test, showing no loss of activity (Figure S34). This result indicates the stability of **1** during OER. UV/Vis and XPS spectra of **1**/CNT further confirmed that the molecular structure of **1** kept unchanged after OER electrolysis (Figures S35 and S36). Importantly, the after-electrolysis **1**/CNT was rinsed with tetrahydrofuran to remove molecules of **1**. The resulted material displayed no signals of Fe in XPS (Figure S37), and showed similar currents as unmodified CNTs in CV measurements (Figure S38). These results together suggested the absence of any heterogeneous FeO$_x$ in the after-electrolysis **1**/CNT and thus suggested the high stability of **1** for OER catalysis. The Faradaic efficiency for O$_2$ generation with **1**/CNT was determined to be $> 98\%$ (Figure 3 f).

In order to address the effect of axial ligand, we investigated OER mechanisms with **1** and **2** using density functional theory (DFT) calculations (Figure 4, computational details are described in the Supporting Information). The ground state of Fe^{III}-OH of **1** is calculated to be doublet with an unpaired electron locating at Fe. From Fe^{III}-OH, a 1e oxidation followed by a deprotonation of Fe-bound hydroxyl take place, giving a formal Fe^{IV}=O species. Importantly, the Fe−O bond length decreases from 1.83 Å in Fe^{III}-OH to 1.66 Å in Fe^{IV}=O (Figure 4 a). In Fe^{IV}=O, two unpaired electrons are each located at Fe and O atoms, and thus it is better described as Fe^{III}-O$^{\bullet}$ radical. Direct hydroxide nucleophilic attack to this Fe^{IV}=O has a calculated free energy barrier of 38.6 kcal mol^{-1} for the O−O bond formation, indicating that the formal Fe^{IV}=O is not likely to undergo this O−O bond formation. Further 1e oxidation of Fe^{IV}=O generates formal [Fe^{V}=O]$^+$ intermediate. DFT studies suggested that porphyrin ligand (denoted as L) is redox-non-
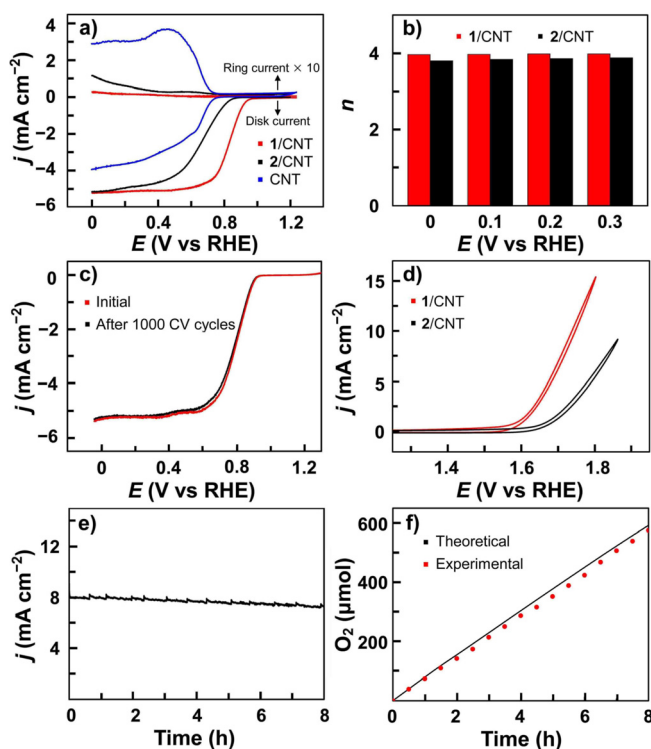

Figure 3. a) RRDE data of **1**/CNT, **2**/CNT, and unmodified CNT with a rotation rate of 1600 rpm. b) ORR n values with **1**/CNT an **2**/CNT as determined by RRDE. c) LSV of **1**/CNT before and after 1000 CV cycles. d) OER CVs of **1**/CNT and **2**/CNT. e) OER electrolysis with **1**/CNT at $\eta = 490\ \mathrm{mV}$. f) Observed and theoretical amounts of O$_2$ produced during electrolysis with **1**/CNT at $\eta = 490\ \mathrm{mV}$.

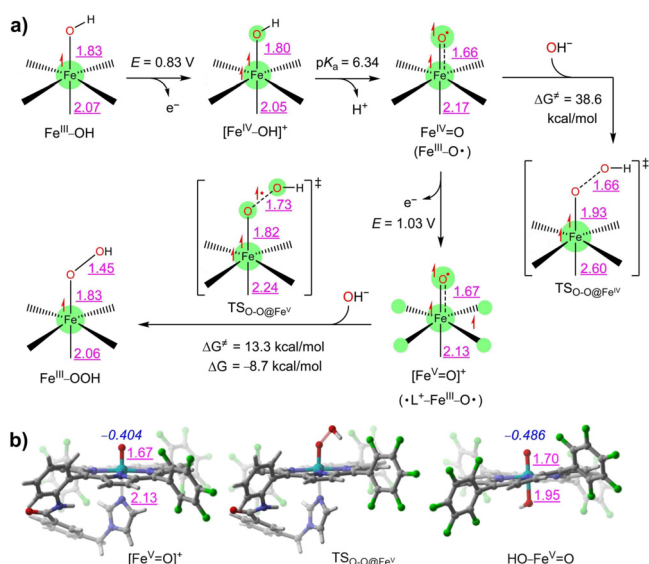**Figure 4.** a) DFT-calculated OER pathway with **1**. b) Optimized structure of formal $[Fe^V=O]^+$ of **1** and its transition state for the O—O bond formation, noted as $TS_{O-O@Fe}{}^V$, and also the structure of HO-$Fe^V=O$ of **2** with a *trans* hydroxide ion on Fe. Dianionic porphyrin ligands are omitted for clarity. Note: Bond lengths in purple underline, spin density distributions in green sphere, unpaired electron in half red arrow, and atomic charge of oxo in italic blue.

innocent. Thus, $[Fe^V=O]^+$ is better described as ·L^+-Fe^{III}-O· diradical. Hydroxide attack to $[Fe^V=O]^+$ has a much smaller free energy barrier of 13.3 kcal mol^{-1} and has an exothermic energy of 8.7 kcal mol^{-1}. Hence, the formal $[Fe^V=O]^+$ species is suggested to be the key intermediate to trigger O—O bond formation.

Unlike **1**, the formal $Fe^V=O$ of **2** will bind a hydroxide ion at its unoccupied *trans* axial site to afford HO-$Fe^V=O$ species (Figure 4b). The calculated exothermic energy is 19.4 kcal mol^{-1}, indicating that the coordination of hydroxide is favoured. Because of the strong electron-pushing effect of negatively charged OH$^-$, the terminal O atom of HO-$Fe^V=O$ in **2** has an atomic charge of -0.486, while this value is only -0.404 for the O atom of $[Fe^V=O]^+$ in **1**. This increased electron density on the terminal O atom of HO-$Fe^V=O$ in **2** makes its O—O bond formation via nucleophilic attack unfavourable. Based on these results, we propose that the tethered imidazole group in **1** is likely to protect the *trans* site of $Fe^V=O$ by preventing the formation of HO-$Fe^V=O$, which is less effective to undergo nucleophilic attack to form O—O bond. It is worth noting that Fe^{III} complexes of tetraamido macrocyclic ligands (TAML) have been shown to be able to catalyze water oxidation with high rates.[39–41] Comparing with Fe porphyrins, Fe TAMLs have stable square planar Fe-N_4 coordination structures without *trans* axial ligands due to the much stronger σ-donating ability of tetraanionic TAML ligands. As a consequence, in the corresponding formal $Fe^V=O$ states, the Fe ions adopt a square pyramidal coordination geometry without *trans* axial ligands.[66,67] This structure is suggested to be critical for Fe TAMLs to undergo efficient O—O bond formation via nucleophilic attack with water or hydroxide.

With high electrocatalytic activity for both ORR and OER, we assembled a Zn-air battery using **1**/CNT (Figure 5a). The resulted battery operates stably and displays a high open-circuit potential of 1.45 V (Figure 5b). For comparison, the battery assembled with **2**/CNT shows a lower open-circuit potential of 1.40 V (Figure S39).

As shown in Figure 5c, at a constant current density of 20 mA cm^{-2}, the specific capacity of battery with **1**/CNT is 785.9 mAh g^{-1}, corresponding to 95.8% of the theoretical capacity of 820 mAh g^{-1} for a Zn-air battery. Note that the specific capacity of Pt/Ir-based battery (assembled using Pt/C-Ir/C) is 757.7 mAh g^{-1}, and it is 696.4 mAh g^{-1} for battery with **2**/CNT (Figure S40). Moreover, the battery with **1**/CNT displays smaller charge/discharge polarization voltages as compared to those with Pt/C-Ir/C (Figure 5d) and with **2**/CNT (Figure S41). The maximum power density of battery with **1**/CNT is 132.9 mW cm^{-2}, which is larger than that with Pt/C-Ir/C (61.6 mW cm^{-2}) and with **2**/CNT (110.8 mW cm^{-2}). As shown in Figure 5e, the battery with **1**/CNT shows a charge/discharge voltage gap of 0.89 V at 2 mA cm^{-2}, which is smaller than that with Pt/C-Ir/C (0.91 V) and with **2**/CNT (0.99 V, Figure S42). Furthermore, at 10 mA cm^{-2}, the charge/discharge voltage gap of **1**/CNT is only 1.10 V (Figure S43). The durability of the battery with **1**/CNT is also examined, showing high stability with almost no degradation throughout 100 cycling tests (Figure 5f). This result is significant to show an unparalleled Zn-air battery assembled with molecular Fe porphyrins, which operates with equal performance to batteries assembled with Pt/Ir-based materials.
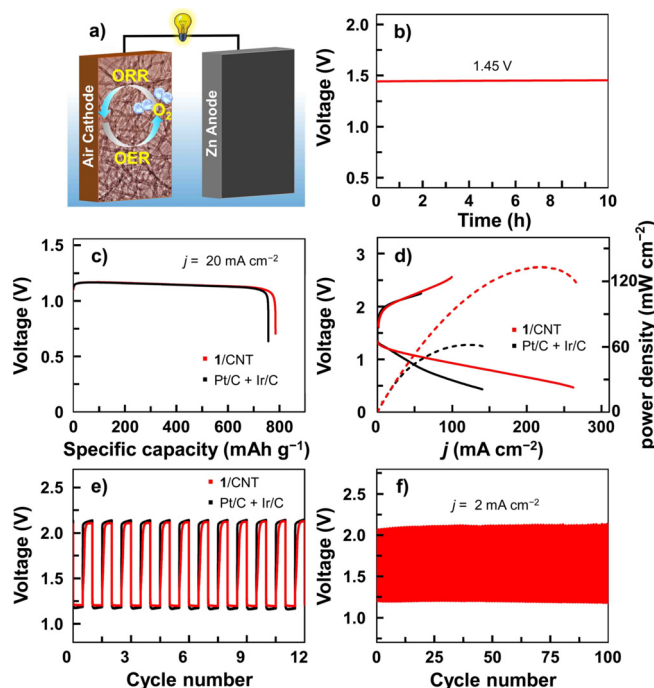

Figure 5. a) Schematic diagram of a Zn-air battery. b) The open-circuit plot of a battery with **1**/CNT. c) Discharge capacity data of batteries with **1**/CNT and Pt/C-Ir/C at a constant current density of 20 mA cm^{-2}. d) Charge/discharge data and their corresponding peak power density data of batteries with **1**/CNT and Pt/C-Ir/C. e) Charge/discharge test of battery with **1**/CNT at current density 2 mA cm^{-2}. f) Long cycling test (20 min per cycle).

Angew. Chem. Int. Ed. **2021**, *60*, 7576–7581

© 2021 Wiley-VCH GmbH

www.angewandte.org **7579**

In conclusion, we report an enzyme-inspired Fe porphyrin **1** as an efficient catalyst for both ORR and OER in alkaline solutions. With a tethered imidazole for Fe binding, **1** significantly beats its imidazole-free analogue **2** for electrocatalytic ORR and OER. For ORR, this axial imidazole can increase electron density on Fe to improve O_2 binding and assist the O−O bond cleavage. For OER, the imidazole group is likely to allow hydroxide attack to $[Fe^V=O]^+$ for the O−O bond formation by protecting the *trans* axial site of $[Fe^V=O]^+$. As a practical demonstration, Zn-air battery assembled with this Fe porphyrin shows equal performance to batteries with Pt/Ir-based materials. This work represents the first example of molecular porphyrin-based Zn-air battery and underlines unique benefits and promising applications of molecular electrocatalysis in new energy technologies.

Conflict of interest

The authors declare no conflict of interest.

Keywords: catalyst design · metal-air battery · molecular electrocatalysis · oxygen evolution · oxygen reduction

[1] M. Wikström, K. Krab, V. Sharma, *Chem. Rev.* **2018**, *118*, 2469–2490.

[2] X. Huang, J. T. Groves, *Chem. Rev.* **2018**, *118*, 2491–2553.

[3] S. M. Adam, G. B. Wijeratne, P. J. Rogler, D. E. Diaz, D. A. Quist, J. J. Liu, K. D. Karlin, *Chem. Rev.* **2018**, *118*, 10840–11022.

[4] S. Dey, B. Mondal, S. Chatterjee, A. Rana, S. Amanullah, A. Dey, *Nat. Rev. Chem.* **2017**, *1*, 0098.

[5] M. L. Pegis, C. F. Wise, D. J. Martin, J. M. Mayer, *Chem. Rev.* **2018**, *118*, 2340–2391.

[6] V. Artero, *Nat. Energy* **2017**, *2*, 17131.

[7] W. Zhang, W. Lai, R. Cao, *Chem. Rev.* **2017**, *117*, 3717–3797.

[8] A. C. Brezny, S. I. Johnson, S. Raugei, J. M. Mayer, *J. Am. Chem. Soc.* **2020**, *142*, 4108–4113.

[9] S. Fukuzumi, Y.-M. Lee, W. Nam, *ChemCatChem* **2018**, *10*, 9–28.

[10] S. Chatterjee, K. Sengupta, S. Hematian, K. D. Karlin, A. Dey, *J. Am. Chem. Soc.* **2015**, *137*, 12897–12905.

[11] S. Bhunia, A. Rana, P. Roy, D. J. Martin, M. L. Pegis, B. Roy, A. Dey, *J. Am. Chem. Soc.* **2018**, *140*, 9444–9457.

[12] M. A. Ehudin, L. Senft, A. Franke, I. Ivanović-Burmazović, K. D. Karlin, *J. Am. Chem. Soc.* **2019**, *141*, 10632–10643.

[13] H. Kitagishi, D. Shimoji, T. Ohta, R. Kamiya, Y. Kudo, A. Onoda, T. Hayashi, J. Weiss, J. A. Wytko, K. Kano, *Chem. Sci.* **2018**, *9*, 1989–1995.

[14] C. Costentin, H. Dridi, J.-M. Savéant, *J. Am. Chem. Soc.* **2015**, *137*, 13535–13544.

[15] C. W. Machan, *ACS Catal.* **2020**, *10*, 2640–2655.

[16] K. M. Kadish, L. Frémond, Z. Ou, J. Shao, C. Shi, F. C. Anson, F. Burdet, C. P. Gros, J.-M. Barbe, R. Guilard, *J. Am. Chem. Soc.* **2005**, *127*, 5625–5631.

[17] N. Levy, A. Mahammed, M. Kosa, D. T. Major, Z. Gross, L. Elbaz, *Angew. Chem. Int. Ed.* **2015**, *54*, 14080–14084; *Angew. Chem.* **2015**, *127*, 14286–14290.

[18] M. Kosa, N. Levy, L. Elbaz, D. T. Major, *J. Phys. Chem. C* **2018**, *122*, 17686–17694.

[19] J. P. Collman, N. K. Devaraj, R. A. Decréau, Y. Yang, Y.-L. Yan, W. Ebina, T. A. Eberspacher, C. E. D. Chidsey, *Science* **2007**, *315*, 1565–1568.

[20] A. Hosseini, C. J. Barile, A. Devadoss, T. A. Eberspacher, R. A. Decreau, J. P. Collman, *J. Am. Chem. Soc.* **2011**, *133*, 11100–11102.

[21] C. T. Carver, B. D. Matson, J. M. Mayer, *J. Am. Chem. Soc.* **2012**, *134*, 5444–5447.

[22] S. Mukherjee, M. Mukherjee, A. Mukherjee, A. Bhagi-Damodaran, Y. Lu, A. Dey, *ACS Catal.* **2018**, *8*, 8915–8924.

[23] P.-J. Wei, G.-Q. Yu, Y. Naruta, J.-G. Liu, *Angew. Chem. Int. Ed.* **2014**, *53*, 6659–6663; *Angew. Chem.* **2014**, *126*, 6777–6781.

[24] P. Nagaraju, T. Ohta, J.-G. Liu, T. Ogura, Y. Naruta, *Chem. Commun.* **2016**, *52*, 7213–7216.

[25] M. L. Rigsby, D. J. Wasylenko, M. L. Pegis, J. M. Mayer, *J. Am. Chem. Soc.* **2015**, *137*, 4296–4299.

[26] R. Götz, K. H. Ly, P. Wrzolek, A. Dianat, A. Croy, G. Cuniberti, P. Hildebrandt, M. Schwalbe, I. M. Weidinger, *Inorg. Chem.* **2019**, *58*, 10637–10647.

[27] S. Chatterjee, K. Sengupta, S. Samanta, P. K. Das, A. Dey, *Inorg. Chem.* **2015**, *54*, 2383–2392.

[28] R. Cao, R. Thapa, H. Kim, X. Xu, M. G. Kim, Q. Li, N. Park, M. Liu, J. Cho, *Nat. Commun.* **2013**, *4*, 2076.

[29] A. Pizarro, G. Abarca, C. Gutiérrez-Cerón, D. Cortés-Arriagada, F. Bernardi, C. Berrios, J. F. Silva, M. C. Rezende, J. H. Zagal, R. Oñate, I. Ponce, *ACS Catal.* **2018**, *8*, 8406–8419.

[30] J. Meng, H. Lei, X. Li, W. Zhang, R. Cao, *J. Phys. Chem. C* **2020**, *124*, 16324–16331.

[31] D. Wang, J. T. Groves, *Proc. Natl. Acad. Sci. USA* **2013**, *110*, 15579–15584.

[32] X. Wang, Z.-F. Cai, D. Wang, L.-J. Wan, *J. Am. Chem. Soc.* **2019**, *141*, 7665–7669.

[33] P. M. Usov, S. R. Ahrenholtz, W. A. Maza, B. Stratakes, C. C. Epley, M. C. Kessinger, J. Zhu, A. J. Morris, *J. Mater. Chem. A* **2016**, *4*, 16818–16823.

[34] J. Sun, J. Yin, P. Liu, Y. Wang, X. Yao, Z. Tang, H. Zhao, *Chem. Sci.* **2016**, *7*, 5640–5646.

[35] Y. Han, Y. Wu, W. Lai, R. Cao, *Inorg. Chem.* **2015**, *54*, 5604–5613.

[36] Y. Liu, Y. Han, Z. Zhang, W. Zhang, W. Lai, Y. Wang, R. Cao, *Chem. Sci.* **2019**, *10*, 2613–2622.

[37] W. Nam, Y.-M. Lee, S. Fukuzumi, *Acc. Chem. Res.* **2014**, *47*, 1146–1154.

[38] M. Okamura, M. Kondo, R. Kuga, Y. Kurashige, T. Yanai, S. Hayami, V. K. K. Praneeth, M. Yoshida, K. Yoneda, S. Kawata, S. Masaoka, *Nature* **2016**, *530*, 465–468.

[39] F. T. de Oliveira, A. Chanda, D. Banerjee, X. Shan, S. Mondal, L. Que, Jr., E. L. Bominaar, E. Münck, T. J. Collins, *Science* **2007**, *315*, 835–838.

[40] E. L. Demeter, S. L. Hilburg, N. R. Washburn, T. J. Collins, J. R. Kitchin, *J. Am. Chem. Soc.* **2014**, *136*, 5603–5606.

[41] C. Panda, J. Debgupta, D. D. Díaz, K. K. Singh, S. S. Gupta, B. B. Dhar, *J. Am. Chem. Soc.* **2014**, *136*, 12273–12282.

7580 www.angewandte.org

© 2021 Wiley-VCH GmbH

Angew. Chem. Int. Ed. **2021**, *60*, 7576–7581

[42] J. L. Fillol, Z. Codolà, I. Garcia-Bosch, L. Gómez, J. J. Pla, M. Costas, *Nat. Chem.* **2011**, *3*, 807–813.

[43] L. D. Wickramasinghe, R. Zhou, R. Zong, P. Vo, K. J. Gagnon, R. P. Thummel, *J. Am. Chem. Soc.* **2015**, *137*, 13260–13263.

[44] L. Xie, X. Li, B. Wang, J. Meng, H. Lei, W. Zhang, R. Cao, *Angew. Chem. Int. Ed.* **2019**, *58*, 18883–18887; *Angew. Chem.* **2019**, *131*, 19059–19063.

[45] B.-Q. Li, C.-X. Zhao, S. Chen, J.-N. Liu, X. Chen, L. Song, Q. Zhang, *Adv. Mater.* **2019**, *31*, 1900592.

[46] M. Yu, Z. Wang, C. Hou, Z. Wang, C. Liang, C. Zhao, Y. Tong, X. Lu, S. Yang, *Adv. Mater.* **2017**, *29*, 1602868.

[47] J. Fu, Z. P. Cano, M. G. Park, A. Yu, M. Fowler, Z. Chen, *Adv. Mater.* **2017**, *29*, 1604685.

[48] X. F. Lu, Y. Chen, S. Wang, S. Gao, X. W. Lou, *Adv. Mater.* **2019**, *31*, 1902339.

[49] D. Chao, C. Ye, F. Xie, W. Zhou, Q. Zhang, Q. Gu, K. Davey, L. Gu, S.-Z. Qiao, *Adv. Mater.* **2020**, *32*, 2001894.

[50] T. Tang, W.-J. Jiang, X.-Z. Liu, J. Deng, S. Niu, B. Wang, S.-F. Jin, Q. Zhang, L. Gu, J.-S. Hu, L.-J. Wan, *J. Am. Chem. Soc.* **2020**, *142*, 7116–7127.

[51] S. Chatterjee, K. Sengupta, S. Samanta, P. K. Das, A. Dey, *Inorg. Chem.* **2013**, *52*, 9897–9907.

[52] D. Sahoo, M. G. Quesne, S. P. de Visser, S. P. Rath, *Angew. Chem. Int. Ed.* **2015**, *54*, 4796–4800; *Angew. Chem.* **2015**, *127*, 4878–4882.

[53] I. Liberman, R. Shimoni, R. Ifraemov, I. Rozenberg, C. Singh, I. Hod, *J. Am. Chem. Soc.* **2020**, *142*, 1933–1940.

[54] D. H. Wang, J. N. Pan, H. H. Li, J. J. Liu, Y. B. Wang, L. T. Kang, J. N. Yao, *J. Mater. Chem. A* **2016**, *4*, 290–296.

[55] J. Guo, X. Yan, Q. Liu, Q. Li, X. Xu, L. Kang, Z. Cao, G. Chai, J. Chen, Y. Wang, J. Yao, *Nano Energy* **2018**, *46*, 347–355.

[56] N. Levy, A. Mahammed, A. Friedman, B. Gavriel, Z. Gross, L. Elbaz, *ChemCatChem* **2016**, *8*, 2832–2837.

[57] A. Friedman, L. Landau, S. Gonen, Z. Gross, L. Elbaz, *ACS Catal.* **2018**, *8*, 5024–5031.

[58] H. C. Honig, C. B. Krishnamurthy, I. Borge-Durán, M. Tasior, D. T. Gryko, I. Grinberg, L. Elbaz, *J. Phys. Chem. C* **2019**, *123*, 26351–26357.

[59] R. Z. Snitkoff, N. Levy, I. Ozery, S. Ruthstein, L. Elbaz, *Carbon* **2019**, *143*, 223–229.

[60] J. S. Shpilman, A. Friedman, N. Zion, N. Levy, D. T. Major, L. Elbaz, *J. Phys. Chem. C* **2019**, *123*, 30129–30136.

[61] K. M. Kadish, J. Shen, L. Frémond, P. Chen, M. El Ojaimi, M. Chkounda, C. P. Gros, J.-M. Barbe, K. Ohkubo, S. Fukuzumi, R. Guilard, *Inorg. Chem.* **2008**, *47*, 6726–6737.

[62] C. C. L. McCrory, S. Jung, J. C. Peters, T. F. Jaramillo, *J. Am. Chem. Soc.* **2013**, *135*, 16977–16987.

[63] X. Li, H. Lei, J. Liu, X. Zhao, S. Ding, Z. Zhang, X. Tao, W. Zhang, W. Wang, X. Zheng, R. Cao, *Angew. Chem. Int. Ed.* **2018**, *57*, 15070–15075; *Angew. Chem.* **2018**, *130*, 15290–15295.

[64] A. Arul, H. Pak, K. U. Moon, M. Christy, M. Y. Oh, K. S. Nahm, *Appl. Catal. B* **2018**, *220*, 488–496.

[65] T. Ghosh, P. Ghosh, G. Maayan, *ACS Catal.* **2018**, *8*, 10631–10640.

[66] M. Z. Ertem, L. Gagliardi, C. J. Cramer, *Chem. Sci.* **2012**, *3*, 1293–1299.

[67] R.-Z. Liao, X.-C. Li, P. E. M. Siegbahn, *Eur. J. Inorg. Chem.* **2014**, 728–741.